RSC Advances

PAPER

View Article Online
View Journal | View Issue

Cite this: *RSC Adv.*, 2026, **16**, 12558

The environmental degradation of naphthalimide, rhodamine and BODIPY fluorophores by hydroxyl radicals: a theoretical insight

Nguyen Linh Nam,[a] Mai Van Bay,[b] Nguyen Thi Hoa,[a] Nguyen Quang Trung,[c] Nguyen Minh Thong,[b] Adam Mechler,[d] Pham Cam Nam,[e] Nguyen Khoa Hien,[f] Duong Tuan Quang[g] and Quan V. Vo *[a]

Rhodamine (**RDA**), naphthalimide (**NPA**), and BODIPY (**BOD**) are widely used fluorophores whose environmental fate is hitherto unexplored. In this study, quantum chemical calculations were employed to investigate the HO•-driven degradation processes of these fluorophores in aqueous and organic media, focusing on the mechanism, kinetics, thermodynamics, and ecological risks. The results suggest that all three fluorophores undergo reactions with HO•, but their behaviors differ markedly. **RDA** displays strong pH-dependent reactivity, with overall rate constants ranging from 8.76×10^8 to 4.02×10^{10} M^{-1} s^{-1} depending on protonation state, and lifetimes spanning from hours to years in natural waters. **NPA** degrades more slowly, with rate constants of 7.06×10^7 M^{-1} s^{-1} (neutral form) and 8.20×10^8 M^{-1} s^{-1} (anion), resulting in greater environmental persistence. **BOD** reacts rapidly across all conditions (4.39×10^9 M^{-1} s^{-1}) consistently *via* RAF mechanism. Temperature and solvent polarity also influence degradation: higher temperatures accelerate all reactions, and methanol enhances reactivity, while lipid-like media reduce degradation rates for **RDA** and **NPA** but not for **BOD**. **NPA**, **RAD** and these intermediates are predicted to exhibit high ecological toxicity ($\log LC_{50}/EC_{50}/ChV < 2$), poor biodegradability, and high bioaccumulation potential, while **BOD** and its products may be comparatively benign. Overall, the hazard ranking is predicted to be **RDA** ≈ **NPA** > **BOD**, with **RDA** posing the highest long-term ecological risk. These findings highlight the need to evaluate not only degradation efficiency but also the toxicity and environmental fate of intermediates when applying advanced oxidation processes for fluorophore removal.

Received 2nd February 2026
Accepted 26th February 2026

DOI: 10.1039/d6ra00906a

rsc.li/rsc-advances

1. Introduction

Fluorophores (**FPHs**) are widely employed in modern chemical, biological, and environmental research principally as labels for observation or sensing.[1–3] Among them, rhodamine (**RDA**),[4–6] naphthalimide (**NPA**),[7–9] and BODIPY (**BOD**)[10–14] are the most important scaffolds that are also frequently derivatized to tune their photophysical properties. Consistently, these scaffolds are frequently used in the design of fluorescent sensors for detecting ions, biomolecules, and environmental pollutants owing to their strong absorption, tunable emission, and chemical versatility.[15,16] Increasing production and use of these compounds have led to the inevitable release of organic contaminants containing **RDA**, **NPA**, and **BOD** motifs into aquatic and terrestrial environments.

Hydroxyl radicals (HO•) are the key transient oxidants in natural surface waters and aquifers due to their exceptionally high reactivity toward organic substrates.[17,18] Consistently their steady-state concentrations are extremely low (typically 10^{-18} to 10^{-15} M), also influenced by temperature, pH, and matrix constituents such as dissolved organic matter (DOM), carbonate/bicarbonate, and halides that can act as radical scavengers or secondary radical sources.[19–21] Due to its high reactivity HO• is consumed at the site of its generation through photochemical processes, and that is the main reason why, even at very low steady state concentrations, HO• plays a decisive role in controlling the environmental fate of biomolecules including industrial chemicals, underpinning the natural self-purification of water.

In contrast, engineered advanced oxidation processes (AOPs) intentionally generate substantially higher transient

[a]*The University of Danang – University of Technology and Education, Danang 550000, Vietnam. E-mail: vvquan@ute.udn.vn*
[b]*The University of Danang – University of Sciences and Education, Danang 550000, Vietnam*
[c]*Quality Assurance and Testing Center 2, Da Nang 550000, Vietnam*
[d]*Department of Biochemistry and Chemistry, La Trobe University, Victoria 3086, Australia*
[e]*The University of Danang – University of Technology and Sciences, Danang 550000, Vietnam*
[f]*Mientrung Institute for Scientific Research, Vietnam National Museum of Nature, Vietnam Academy of Science and Technology, Hue 530000, Vietnam*
[g]*Department of Chemistry, Hue University, Hue 530000, Vietnam*

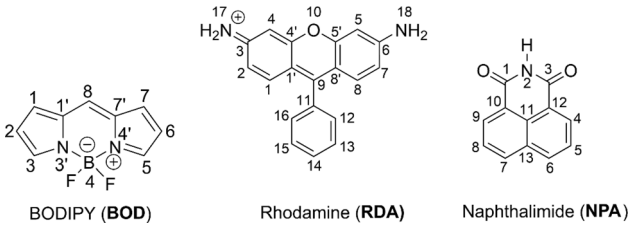

Fig. 1 Structure of fluorophores (FPHs).

concentrations of reactive oxygen species (ROS), including $HO^{\bullet}$, $SO_4^{\bullet-}$, $Cl^{\bullet}$, $ClO^{\bullet}$, $HOO^{\bullet}$ and $O_2^{\bullet-}$ to enhance contaminant degradation. Among these, $HO^{\bullet}$ is also regarded as the predominant oxidant responsible for organic transformation.[22–24] Through single-electron transfer, hydrogen abstraction, and radical addition mechanisms, $HO^{\bullet}$ can initiate complex degradation pathways that may convert relatively benign fluorophores into more reactive or potentially toxic intermediates. Therefore, a comprehensive environmental safety assessment requires not only evaluation of the parent compounds but also a mechanistic understanding of their $HO^{\bullet}$-induced degradation pathways and products under clearly defined environmental and treatment scenarios.

To date, however, systematic studies on the degradation mechanisms and ecological toxicity of the intermediates derived from **RDA**, **NPA**, and **BOD** (Fig. 1) have not been reported. This knowledge gap is critical, as these fluorophores are structurally diverse and may exhibit different degradation behaviors, reactivities, and risks. Comprehensive mechanistic insights are therefore needed to assess both their environmental persistence and the potential ecological hazards of their transformation products.

In recent years, computational chemistry has reached a level of predictive accuracy that allows its use as a tool for exploring experimentally challenging chemical processes, such as environmental degradation pathways,[25–30] delivering reliable predictions of thermodynamics, kinetics, as well as toxicity of the byproducts. In this study, we employed state-of-the-art computational approaches to investigate the degradation of **RDA**, **NPA**, and **BOD** by hydroxyl radicals in aqueous solution, as well as their relevance to sensor applications in biological and lipid-like environments, with a particular focus on elucidating their mechanistic pathways and assessing the toxicity of major intermediates. This work provides the first systematic evaluation of these important fluorophores, linking molecular reactivity with environmental risk.

2. Computational methods

All calculations were performed using Gaussian 16 at the M062X/6-311++G(d,p) level of theory.[31] This approach has been demonstrated to provide reliable thermodynamic and kinetic parameters for radical reactions.[32–38] Solvent effects in water were described using the SMD implicit solvation model,[32] which is widely applied in studies of radical reactions. The protocol has been validated against experimental data, typically affording $k_{calc.}/k_{exp.}$ ratios between 0.3 and 2.9.[34,39–43] Although improved treatments of intramolecular rotational contributions have been suggested,[44] the Quantum Mechanics-based Overall Free Radical Scavenging Activity (QM-ORSA) method[43] was adopted to balance computational cost and accuracy for the present system. Accordingly, kinetic parameters were determined within the QM-ORSA method.[34,43,45] Under standard conditions of 1 M concentration and varying ambient temperatures (273–373 K for water), the rate constant (k) was determined using eqn (1) and transition state theory (TST) and details in Table S1, SI.[41,46–51]

$$k = \sigma\kappa\frac{k_B T}{h}e^{-(\Delta G^{\ddagger})/RT} \quad (1)$$

The Gibbs free energy of activation is denoted as $\Delta G^{\ddagger}$, while k_B and h represent the Boltzmann constant and Planck constant, respectively. Tunneling corrections (κ), were computed using the Eckart barrier model.[52] σ stands for the reaction symmetry number.[53,54]

The radical adduct formation (RAF), single electron transfer (SET), or formal hydrogen transfer (FHT) pathways detailed in eqn (2)–(4) can provide the mechanistic underpinning of the reaction between **FPHs** and $HO^{\bullet}$, with consideration to the molecular structure:[34,41,45,55–58]

$$\text{RAF: FPHs-H} + HO^{\bullet} \rightarrow [\text{HO-FPHs-H}]^{\bullet} \quad (2)$$

$$\text{SET: FPHs-H} + HO^{\bullet} \rightarrow [\text{FPHs-H}]^{\bullet+} + HO^{-} \quad (3)$$

$$\text{FHT: FPHs-H} + HO^{\bullet} \rightarrow \text{FPHs}^{\bullet} + H_2O \quad (4)$$

The ecotoxicological potential was predicted using the Ecological Structure–Activity Relationship model (ECOSAR V2.0), which has been extensively validated for assessing the aquatic toxicity of organic compounds.[59–63] Bioconcentration factors (BCFs) of the transformation products derived from **FPH** degradation were estimated with the BCFBAF module implemented in the EPI Suite™ package.[64] In addition, the biodegradation behavior of **FPHs** and their corresponding degradation products was evaluated using the BIOWIN 3, 4, and 5 submodels available within EPI Suite™.[64] For computational consistency, radical intermediates were converted into their hydrogen-saturated closed-shell forms prior to prediction.

3. Results and discussion

3.1. The reaction of fluorophores with $HO^{\bullet}$ in water

3.1.1. Deprotonation. In natural aquatic systems, the protonation equilibria of **RDA** and **NPA** determine their speciation profiles and strongly influence their reactivity toward hydroxyl radicals. For **RDA**, the pK_a values ($pK_{a1} = 2.93$; $pK_{a2} = 6.69$) indicate two successive deprotonation steps (Fig. 2a). At acidic pH (<3), **RDA-H_2A** is the dominant species. In the pH = 3–6, the equilibrium shifts toward the **RDA-HA** form, which becomes the major contributor. Under alkaline conditions (pH ≥ 7), the neutral **RDA** form progressively dominates, reaching over 95% at pH 8. This pH-dependent distribution

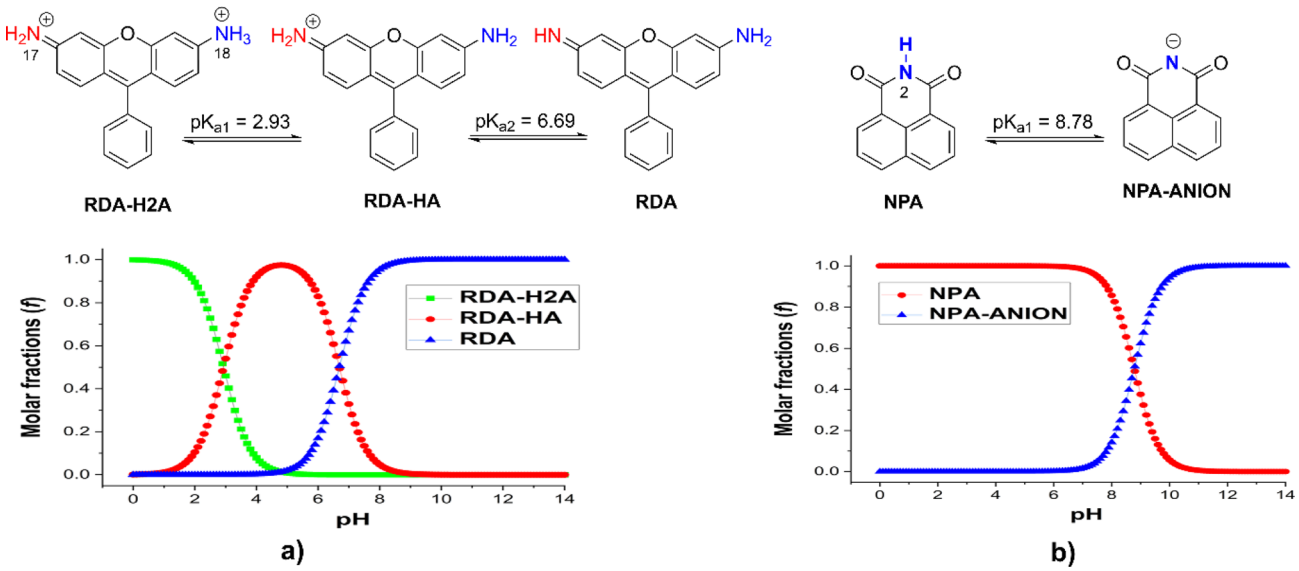

Fig. 2 The deprotonation and molar fractions of RDA (a) and NPA (b) (the results were obtained *via* the Chemaxon code).[65]

highlights that **RDA** will mostly exist as the neutral form at pH > 8, which modifies its solvation and electronic distribution and thus its susceptibility to radical attack.

By contrast, **NPA**, with a single weakly acidic site ($pK_a = 8.78$), remains almost entirely in the neutral state throughout acidic to near-neutral pH (Fig. 2b). Only under mildly alkaline conditions does the anionic species emerge, becoming significant around its pK_a. Thus, unlike **RDA**, **NPA** shows little speciation change in natural waters, and its reactivity toward hydroxyl radicals will be governed largely by its intrinsic neutral electronic structure. The results show that **BOD** does not undergo proton dissociation and therefore maintains a constant molecular form across the environmental pH range. Compared with **RDA** and **NPA**, this absence of speciation effects implies that its degradation kinetics are independent of pH and controlled mainly by inherent electronic properties.

Accordingly, **RDA** is highly sensitive to environmental pH through its stepwise deprotonation equilibria, while **NPA** and **BOD** remain largely invariant under neutral conditions. This difference provides a clear mechanistic basis for the distinct environmental degradation pathways expected for these fluorophores. Thus, the degradation processes of **RAD** and **NPA** in aqueous solution will be evaluated under their deprotonated forms, whereas that of **BOD** will be excluded from consideration.

3.1.2. Thermal evaluation. The calculated $\Delta G°$ (kcal mol^{-1}) of the reactions between **FPHs** and HO$^{\bullet}$ radical *via* the formal hydrogen transfer (FHT), radical adduct formation (RAF), and single electron transfer (SET) pathways at 298.15 K in water are summarized in Table 1. These data provide a thermodynamic basis for assessing the dominant degradation mechanisms of the studied fluorophores under environmentally relevant conditions.

For **RDA**, the protonation state strongly modulates the reaction thermodynamics. In the diprotonated (**RDA-H_2A**) and monoprotonated (**RDA-HA**) forms, FHT at N–H bonds are highly exergonic, with $\Delta G°$ values down from −13.9 to −35.6 kcal mol^{-1}. In neutral form (**RDA**), FHT at N17–H remains strongly favorable ($\Delta G° = -28.4$ kcal mol^{-1}), while RAF at conjugated carbon centers such as C9 ($\Delta G° = -31.6$ kcal mol^{-1}) and C2 ($\Delta G° = -22.9$ kcal mol^{-1}) also becomes competitive, consistent with the dual H-abstraction/addition accessibility seen in aromatic compounds.[30,66,67] RAF at nitrogen sites, however, is endergonic (positive $\Delta G°$), supporting the role of N atoms as H-donors rather than radical-addition sites.

NPA exhibits a markedly different profile. For the neutral form, the Gibbs free energy of FHT(N2–H) is nearly zero, suggesting a limited driving force for hydrogen abstraction. Instead, RAF provides the dominant route, with favorable addition at C6/C7 ($\Delta G° = -17.0$ kcal mol^{-1}) and C4/C9 ($\Delta G° = -12.4$ kcal mol^{-1}). Deprotonation to the **NPA-ANION** slightly enhances the exergonicity of RAF, whereas SET remains energetically unfavorable ($\Delta G° = 13.6$ kcal mol^{-1}). Such carbon-centered RAF as the major degradation route parallels findings for oxidation of phenols and aromatic amino acids by $^{\bullet}$OH.[68,69] However, the thermodynamic profile is markedly different in the **BOD**. FHT is strongly unfavorable ($\Delta G° = 70.9$ kcal mol^{-1}) and SET is marginally accessible ($\Delta G° = 8.8$ kcal mol^{-1}). In contrast, the RAF pathway at several aromatic carbons is highly exergonic. Specifically, the calculated $\Delta G°$ values are −32.4 kcal mol^{-1} at C5 and −32.2 kcal mol^{-1} at C3, indicating that RAF is the dominant thermodynamically favored pathway. This agrees with computational studies on methyl *N*-(3,4-dichlorophenyl)carbamate and oxcarbazepine degradation, where radical addition at electron-rich aromatic carbons drives degradation.[28,30]

Thus, the findings reveal distinct thermodynamic characteristics among the studied compounds. **RDA** can undergo either FHT or RAF mechanisms depending on its protonation state, whereas **NPA** proceeds *via* both RAF and FHT mechanisms. In contrast, **BOD** is predominantly degraded through the RAF pathway. The consistently unfavorable SET process

Table 1 The calculated $\Delta G°$ (kcal mol^{-1}) of the reaction between **FPHs** with HO$^{\bullet}$ radical following the FHT, RAF and SET pathways at 298.15 K in water

Mechanisms	Positions	**BOD**	**RDA-H_2A**	**RDA-HA**	**RDA**	**NPA**	**NPA-ANION**
FHT	B–F	70.9					
	N2–H					0.0	
	N17–H		−13.9	−19.9	−28.4		
	N18–H		−35.6	−19.9			
RAF	C1	−26.6	−13.3	−9.7	−15.3		6.7
	C1′	−10.3	−4.9	3.1	−11.4		
	C2	−14.3	−17.8	−13.3	−22.9		
	C3	−32.2	0.5	−4.4	−5.3		
	C4		−13.1	−8.9	−19.7	−12.4	−12.5
	C4′		−10.7	−6.5	−16.7		
	C5	−32.4	−10.9	−8.3	−10.0	−7.3	−8.0
	C5′		−12.2	−6.3	−18.6		
	C6	−14.4	−16.4	−4.2	−12.9	−17.0	−17.8
	C7	−26.2	−7.0	−12.8	−10.3	−17.0	−17.8
	C7′	−10.4			−10.9		
	C8	−9.0	−13.4	−10.2	−0.4	−7.3	−8.0
	C8′		6.0	0.4	−15.3		
	C9		−23.3	−15.4	−31.6	−12.4	−12.5
	C10					−4.8	−7.6
	C11		−4.9	−0.4	−0.4	9.0	8.7
	C12		−6.9	−6.6	−6.6	−4.8	−7.6
	C13		−5.8	−5.9	−5.9	10.1	9.6
	C14		−8.7	−7.6	−7.4		
	C15		−5.8	−6.0	−6.0		
	C16		−6.9	−6.7	−6.7		
	N3′	26.8					
	N4′	27.0					
	N17		12.4	19.7	29.6		
	N18			19.6	−10.6		
SET		8.8	24.3	9.7	−9.5	25.0	13.6

indicates its minor role in aqueous media, apart from the **NPA-ANION** state. These thermodynamic insights establish a mechanistic basis for assessing and predicting the environmental degradation behaviors of fluorophores under hydroxyl radical attack.

3.1.3. Kinetic evaluation. The kinetic analysis of hydroxyl radical attack on the studied fluorophores in aqueous solution reveals strong mechanistic dependence on both molecular structure and protonation state. The detailed data, including activation free energies ($\Delta G^{\ddagger}$), tunneling corrections (k), branching ratios (Γ), and rate constants (k_{Eck} and $k_{overall}$), are presented in Table 2 for **BOD/NPA** and Table 3 for **RDA**. The corresponding dominant pathways and their relative product distributions are illustrated in Fig. 3 (**BOD/NPA**) and Fig. 4 (**RDA**).

Table 2 Calculated $\Delta G^{\ddagger}$ (kcal mol^{-1}), rate constants (k_{Eck} and $k_{overall}$ M^{-1} s^{-1}), k and Γ of the reaction between HO$^{\bullet}$ and **BOD/NPA** reactions at 298.15 K in water

		BOD			**NPA**					
					NPA			**NPA-ANION**		
Mechanisms		$\Delta G^{\ddagger}$	k_{app}	Γ	$\Delta G^{\ddagger}$	k_{app}	Γ	$\Delta G^{\ddagger}$	k_{app}	Γ
FHT	N2–H				25.2	2.00×10^{-6}	0.0			
RAF	C1	5.8	6.40×10^{8}	14.6						
	C1′	5.2	1.10×10^{9}	25.0						
	C2	6.4	2.50×10^{8}	5.7						
	C3	3.7	2.40×10^{9}	54.6						
	C4				8.7	7.00×10^{6}	9.9	7.2	7.10×10^{7}	8.7
	C5				9.4	2.00×10^{6}	2.8	5.9	5.30×10^{8}	1.1
	C6				7.4	5.60×10^{7}	79.3	6.5	2.10×10^{8}	64.6
	C8	8.6	3.20×10^{6}	0.1						0.0
	C10				8.3	5.60×10^{6}	7.9	6.5	2.10×10^{8}	25.6
$k_{overall}$			**4.39×10^{9}**			**7.06×10^{7}**			**8.20×10^{8}**	

Table 3 Calculated $\Delta G^{\ddagger}$ (kcal mol^{-1}), rate constants (k_{app} and $k_{overall}$ M^{-1} s^{-1}), k and Γ of the reaction between HO$^{\bullet}$ and **RDA** reactions at 298.15 K in water

		RDA-H$_2$A			**RDA-HA**			**RDA**		
Mechanism		$\Delta G^{\ddagger}$	k_{app}	Γ (%)	$\Delta G^{\ddagger}$	k_{app}	Γ (%)	$\Delta G^{\ddagger}$	k_{app}	Γ (%)
SET								1.0	8.50×10^{9}	21.2
FHT	N17–H	20.6	9.90×10^{-3}	0.0	4.9	2.00×10^{9}	37.5			0.0
	N18–H	25.0	2.50×10^{1}	0.0				≈0	2.80×10^{9}	7.0
RAF	C1	8.8	2.70×10^{6}	0.3	9.1	3.40×10^{6}	0.1	5.2	7.20×10^{8}	1.8
	C1′	10.7	1.10×10^{5}	0.0				1.3	2.60×10^{9}	6.5
	C2	6.8	7.40×10^{7}	8.4	5.3	1.00×10^{9}	18.8	2.6	2.60×10^{9}	6.5
	C3	13.2	1.40×10^{3}	0.0	11.4	6.80×10^{4}	0.0	9.4	9.00×10^{5}	0.0
	C4	5.1	7.70×10^{8}	87.9	3.7	2.30×10^{9}	43.1	≈0	2.80×10^{9}	7.0
	C4′	10.2	2.50×10^{5}	0.0	11.4	7.10×10^{4}	0.0	2.5	2.30×10^{9}	5.7
	C5	7.9	1.30×10^{7}	1.5				1.9	2.70×10^{9}	6.7
	C5′	11.7	2.50×10^{4}	0.0				2.2	2.30×10^{9}	5.7
	C6	10.3	2.60×10^{5}	0.0				3.8	2.60×10^{9}	6.5
	C7	9.6	7.50×10^{5}	0.1				3.0	2.20×10^{9}	5.5
	C8	9.4	1.20×10^{6}	0.1				6.0	2.50×10^{8}	0.6
	C8′	14.5	1.90×10^{2}	0.0				2.1	2.60×10^{9}	6.5
	C9	11.0	7.00×10^{4}	0.0	11.8	1.70×10^{4}	0.0	0.3	2.60×10^{9}	6.5
	C11	16.1	1.30×10^{1}	0.0	16.1	1.20×10^{1}	0.0	15.9	1.80×10^{1}	0.0
	C12	8.4	1.10×10^{7}	1.3	7.9	2.40×10^{7}	0.5	7.9	1.20×10^{7}	0.0
	C13	9.5	1.60×10^{6}	0.2	9.2	2.60×10^{6}	0.0	23.4	2.20×10^{-15}	0.0
	C14	9.4	1.00×10^{6}	0.1	9.1	1.50×10^{6}	0.0	8.5	3.90×10^{6}	0.0
	N17							1.5	2.60×10^{9}	6.5
$k_{overall}$			**8.76×10^{8}**			**5.33×10^{9}**			**4.02×10^{10}**	

The **BOD** + HO$^{\bullet}$ reaction only occurred following the RAF mechanism. The major pathway was C3 addition forming **B-P3** ($\Delta G^{\ddagger}$ = 3.7 kcal mol^{-1}, Γ = 54.6%, $k = 2.40 \times 10^{9}$ M^{-1} s^{-1}, Fig. 3). Significant secondary products included **B-P1′** ($\Delta G^{\ddagger}$ = 5.2 kcal mol^{-1}, Γ = 25%, $k = 1.10 \times 10^{9}$ M^{-1} s^{-1}), **B-P1** ($\Delta G^{\ddagger}$ = 5.8 kcal mol^{-1}, Γ = 14.6%, $k = 6.40 \times 10^{8}$ M^{-1} s^{-1}), and **B-P2** ($\Delta G^{\ddagger}$ = 6.4 kcal mol^{-1}, Γ = 5.7%, $k = 2.50 \times 10^{8}$ M^{-1} s^{-1}). With $k_{overall} = 4.39 \times 10^{9}$ M^{-1} s^{-1}, **BOD** was consumed rapidly by HO$^{\bullet}$ despite the absence of any contributions of the FHT and SET reactions.

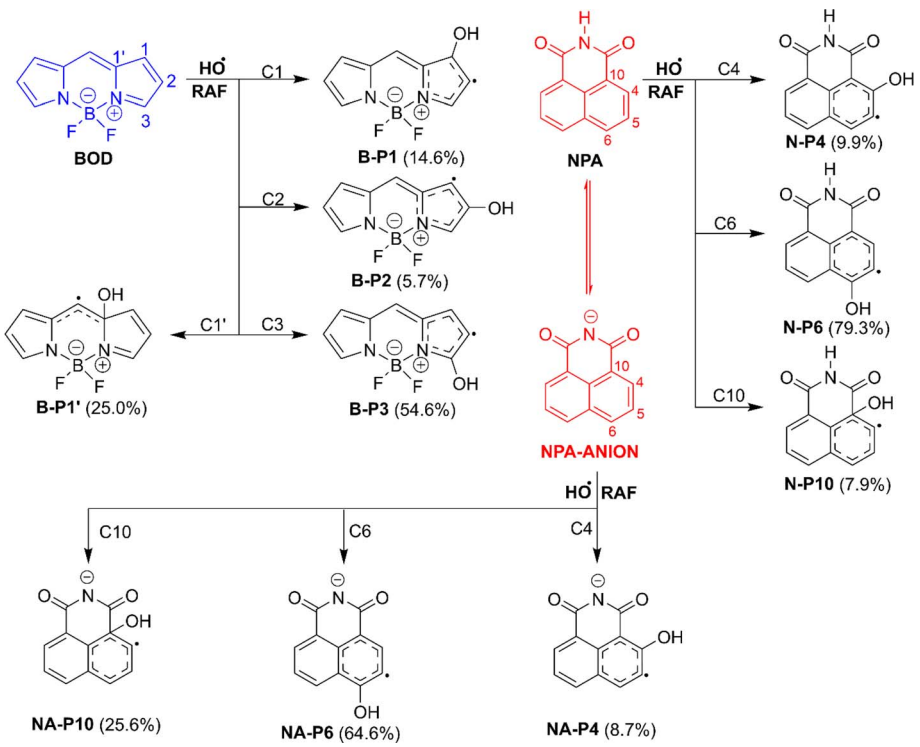

Fig. 3 The dominant mechanisms and % products (Γ > 5%) of the HO$^{\bullet}$ + BOD/NPA reactions in water at 298.15 K.

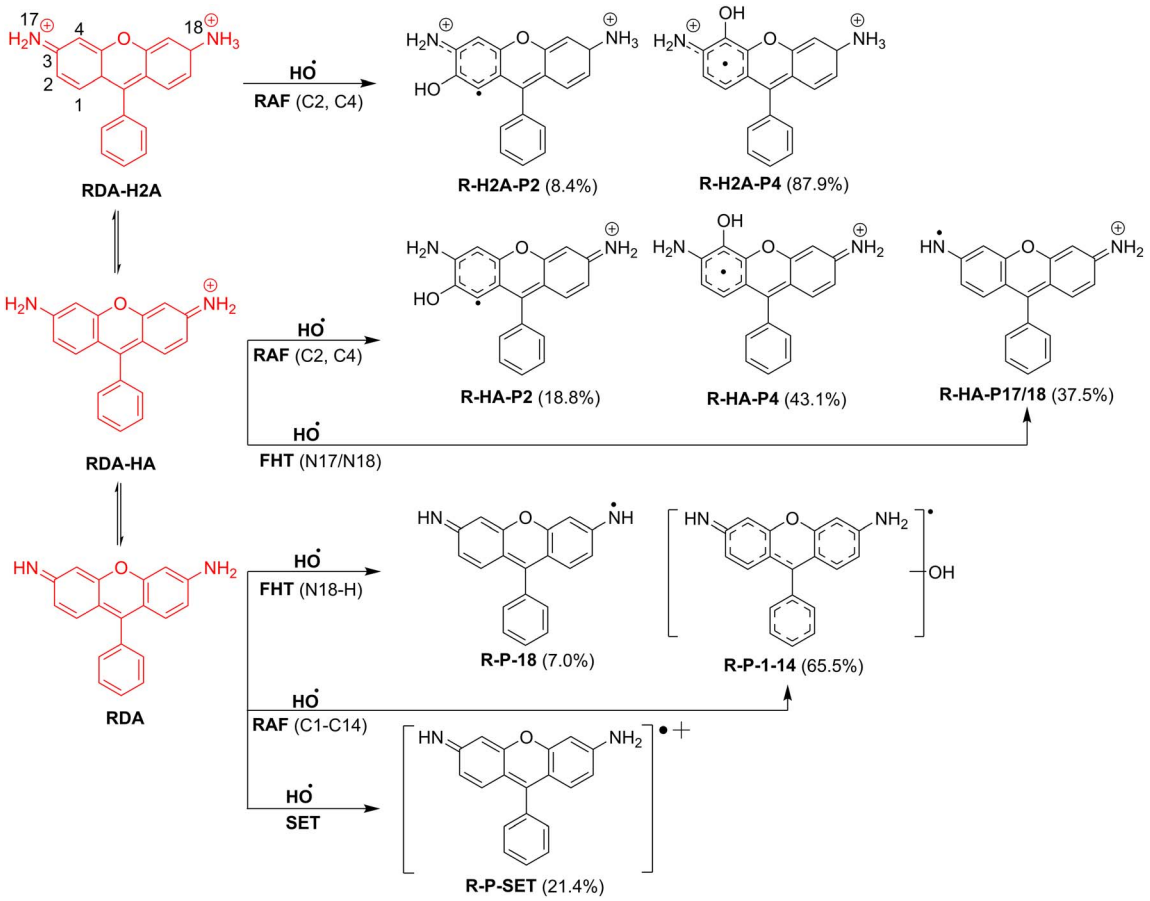

Fig. 4 The dominant mechanisms and % products (Γ > 5%) of the HO• + RDA reactions in water at 298.15 K.

Studying the degradation of **NPA** indicated that the neutral form reacted moderately with HO•, characterized by a dominant RAF pathway at C6 forming **N-P6** ($\Delta G^{\ddagger}$ = 7.4 kcal mol^{-1}, Γ = 79.3%, $k = 5.60 \times 10^{7}$ M^{-1} s^{-1}, Fig. 3) and minor contributions from **N-P4** (C4 addition, $\Delta G^{\ddagger}$ = 8.7 kcal mol^{-1}, Γ = 9.9%, $k = 7.00 \times 10^{6}$ M^{-1} s^{-1}) and **N-P10** (C10 addition, $\Delta G^{\ddagger}$ = 8.3 kcal mol^{-1}, Γ = 7.9%, $k = 5.60 \times 10^{6}$ M^{-1} s^{-1}). Its overall rate constant (7.06×10^{7} M^{-1} s^{-1}) was below the fast degradation threshold, indicating medium reactivity and comparatively higher environmental persistence. Deprotonation to the **NPA-ANION**, however, increased the reactivity substantially, raising the overall rate to 8.20×10^{8} M^{-1} s^{-1}. The RAF reaction was still favored for the anion state with a broader distribution (**N-P6**, Γ = 64.6%, $k = 2.10 \times 10^{8}$ M^{-1} s^{-1}) and remained dominant, while **N-P10** (Γ = 25.6%, $k = 2.10 \times 10^{8}$ M^{-1} s^{-1}) became a significant secondary pathway.

As presented in Table 3, the overall rate constant for the **RDA-H$_2$A** + HO• reaction was the lowest, at 8.76×10^{8} M^{-1} s^{-1}, while that for the **RDA** + HO• reaction was the highest, reaching 4.02×10^{10} M^{-1} s^{-1}. The **RDA-HA** + HO• reaction exhibited an intermediate reactivity, with an overall rate constant of 5.33×10^{9} M^{-1} s^{-1}.

The most favorable pathway of the **RDA-H$_2$A** + HO• reaction was RAF at C4, yielding the intermediate **R-H$_2$A-P4** ($k = 7.70 \times 10^{8}$ M^{-1} s^{-1}, Γ = 87.9%, Fig. 4). A secondary pathway at C2 ($\Delta G^{\ddagger}$ = 6.8 kcal mol^{-1}) produced **R-H$_2$A-P2** (Γ = 8.4%, $k = 7.40 \times 10^{7}$ M^{-1} s^{-1}). In contrast, the **RDA-HA** + HO• reaction was defined by both the FHT and RAF reactions. The FHT at N–H ($\Delta G^{\ddagger}$ = 4.9 kcal mol^{-1}) lead to **R-HA-P17/18** (Γ = 37.5%, $k = 2.00 \times 10^{9}$ M^{-1} s^{-1}), whereas the RAF at C4 ($\Delta G^{\ddagger}$ = 3.7 kcal mol^{-1}) yielded **R-HA-P4** (Γ = 43.1%, $k = 2.30 \times 10^{9}$ M^{-1} s^{-1}) and at C2 ($\Delta G^{\ddagger}$ = 5.3 kcal mol^{-1}) formed **R-HA-P2** (Γ = 18.8%, $k = 1.00 \times 10^{9}$ M^{-1} s^{-1}). Unlike the protonated species, neutral **RDA** distributed reactivity across a broad set of RAF pathways, each contributing between 1.8 and 7.0% to the branching ratio with $k = 7.20 \times 10^{8}$ to 2.80×10^{9} M^{-1} s^{-1}. In addition, the SET pathway produced **R-P-SET** with a substantial contribution (Γ = 21.2%, $k = 8.50 \times 10^{9}$ M^{-1} s^{-1}). This mechanistic expansion underscored the influence of deprotonation, which opened multiple parallel decay routes and significantly accelerated degradation.

The results show that protonation state governed the degradation mechanisms. The defining mechanism of the **RDA** degradation shifted from selective RAF to mixed FHT/RAF and finally to RAF/SET with deprotonation. **NPA** remained RAF-controlled but became more reactive, and **BOD** was also consistently RAF-dominated. Overall, deprotonation enhanced reactivity and influenced fluorophore stability under hydroxyl radical attack.

3.1.4. The effects of pH on the degradation. The degradation of **RDA** and **NPA** by hydroxyl radicals shows a marked

dependence on pH, while **BOD** remains unaffected since it does not undergo proton dissociation. The molar fractions of the individual species were calculated using conventional acid–base equilibrium expressions. While uncertainties in the reported pK_a values may moderately affect the predicted species distributions and log($k_{overall}$), such deviations are expected to impose limited and approximately symmetric influences, and therefore do not materially alter the overall kinetic trends or mechanistic conclusions. Fig. 5a illustrates the pH–log($k_{overall}$) relationships, and Fig. 5b and c depict the evolution of branching ratios (Γ, %) of the main intermediates as a function of pH.

It was observed that proton dissociation exerts a pronounced influence on the reactivity of **RDA**. At pH values below 2, where the diprotonated form (**RDA-H_2A**) predominated, the overall rate constant remained relatively low (log($k_{overall}$) = 8.9–9.1). However, as the pH increased to the range of 2.0–8.7, the log($k_{overall}$) rose by approximately 1.5 units, subsequently stabilizing at 10.6 for pH > 8.7.

This steep rise reflects the combined effect of expanded RAF channels and the additional SET contribution available in the neutral form. Concomitantly, the branching ratios changed from a highly selective RAF pathway at C4 (**R-H_2A-P4**, Fig. 5c) in acidic solution, to a mixed FHT/RAF reaction (**R-HA-P17/18**, **R-HA-P4**, **R-HA-P2**) under mildly acidic–neutral conditions, and finally to a diversified RAF and SET reactions at higher pH, with multiple intermediates (**R-P-SET**, **R-P-18**, **R-P-(1–14)**) contributing more than 5%. Thus, higher pH values favored both faster overall degradation and a broader distribution of intermediate products.

For **NPA**, the neutral form (**NPA-HA**) dominated under acidic to neutral conditions, yielding log($k_{overall}$) = 7.8 and moderate reactivity. In this condition, RAF at C6 (**N-P6**) was the dominant product (>79%, Fig. 5b), with minor contributions from C4 (**N-P4**) and C10 (**N-P10**). As the pH increased toward alkaline conditions, deprotonation occurred, forming the **NPA-ANION**. This transition substantially accelerated the reaction, with log($k_{overall}$) rising above 8.9 and entering the fast-degradation domain. The product distribution also broadened: while **NA-P6** remained the major intermediate (≈65%), **NA-P10** increased to ≈25%, and **NA-P4** retained ≈9%. The reduction of activation barriers upon deprotonation thus explained both the enhancement in rate constants and the redistribution of branching ratios.

From an applied perspective, these findings suggest that water treatment processes based on hydroxyl radicals (*e.g.*, advanced oxidation processes) should be optimized at mildly alkaline conditions to ensure efficient removal of both compounds. While **RDA** will degrade readily across a broad pH window, achieving effective decomposition of **NPA** requires a shift toward alkaline environments. This distinction emphasizes the necessity of pH control in designing advanced oxidation protocols targeting fluorophore contaminants.

3.1.5. The effects of temperature on the degradation of typical states. To evaluate the effect of temperature on the degradation of the representative fluorophores, the rate constants for the reactions of the typical **FPHs**, including **BOD**, **RDA-HA**, and **NPA** with HO˙ were calculated in the range of 273–373 K (Fig. 6a). In all cases, the rate constants (log(k)) increased as the temperature rose, although the magnitude of this enhancement varied among the three compounds.

As illustrated in Fig. 6a1–6a3, the overall rate constant (log($k_{overall}$)) for the reaction between **BOD** and HO˙ radicals exhibited a moderate increase from 9.4 to 9.9, indicating that the RAF processes at the C1, C3, and C1′ sites remained predominant throughout the investigated temperature range. For the **RDA-HA** compound, log($k_{overall}$) increased by approximately 0.5 unit, primarily due to the synergistic contributions of the FHT(N17–H) and the RAF at the C2 and C4 positions. In contrast, the reaction of **NPA** with HO˙ radicals displayed only a slight variation in log($k_{overall}$), ranging from 7.8 to 8.1 within the 273–373 K.

As the temperature increased, the branching ratios of the principal intermediates exhibited systematic changes (Fig. 6b). In the case of **BOD**, the predominant intermediate (**B-P3**) increased markedly by 25.6%, whereas **B-P1′** and **B-P1** showed moderate declines from 28.0% to 15.6% and from 19.0% to 10.4%, respectively. For the **RDA-HA** state, the RAF product at the C4 position (**R-HA-P4**) rose from 39.3% to 55.0%, while the FHT (**R-HA-P17/18**) and RAF (**R-HA-P2**) products decreased slightly by 3.2 and 12.3 percentage units, respectively, indicating that the RAF(C4) pathway became increasingly favored at elevated temperatures. In contrast, **NPA** exhibited persistent selectivity toward the C6 pathway (**N-P6**), which remained the

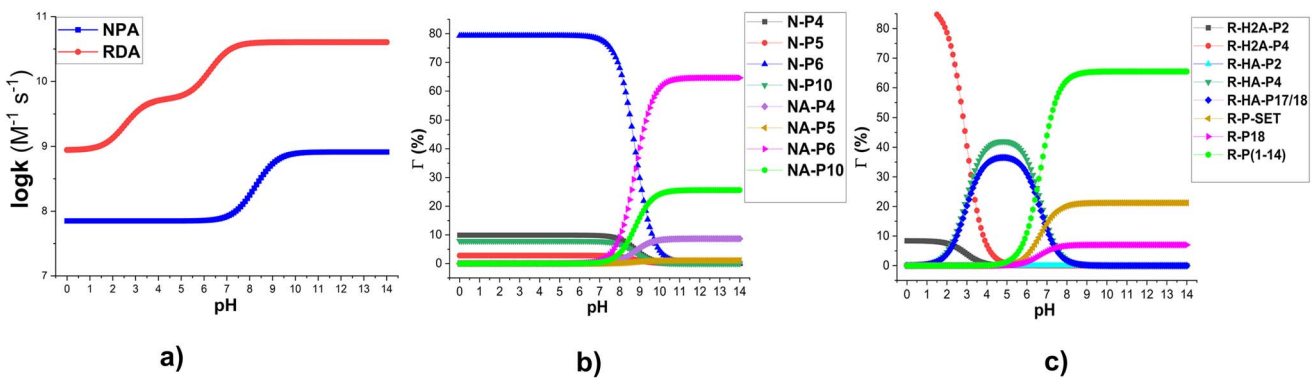

Fig. 5 The log($k_{overall}$) (a) and the branching ratios (Γ, %) of the main products of the NPA (b)/RDA (c) + HO˙ reactions in water following the pH values at 298.15 K.

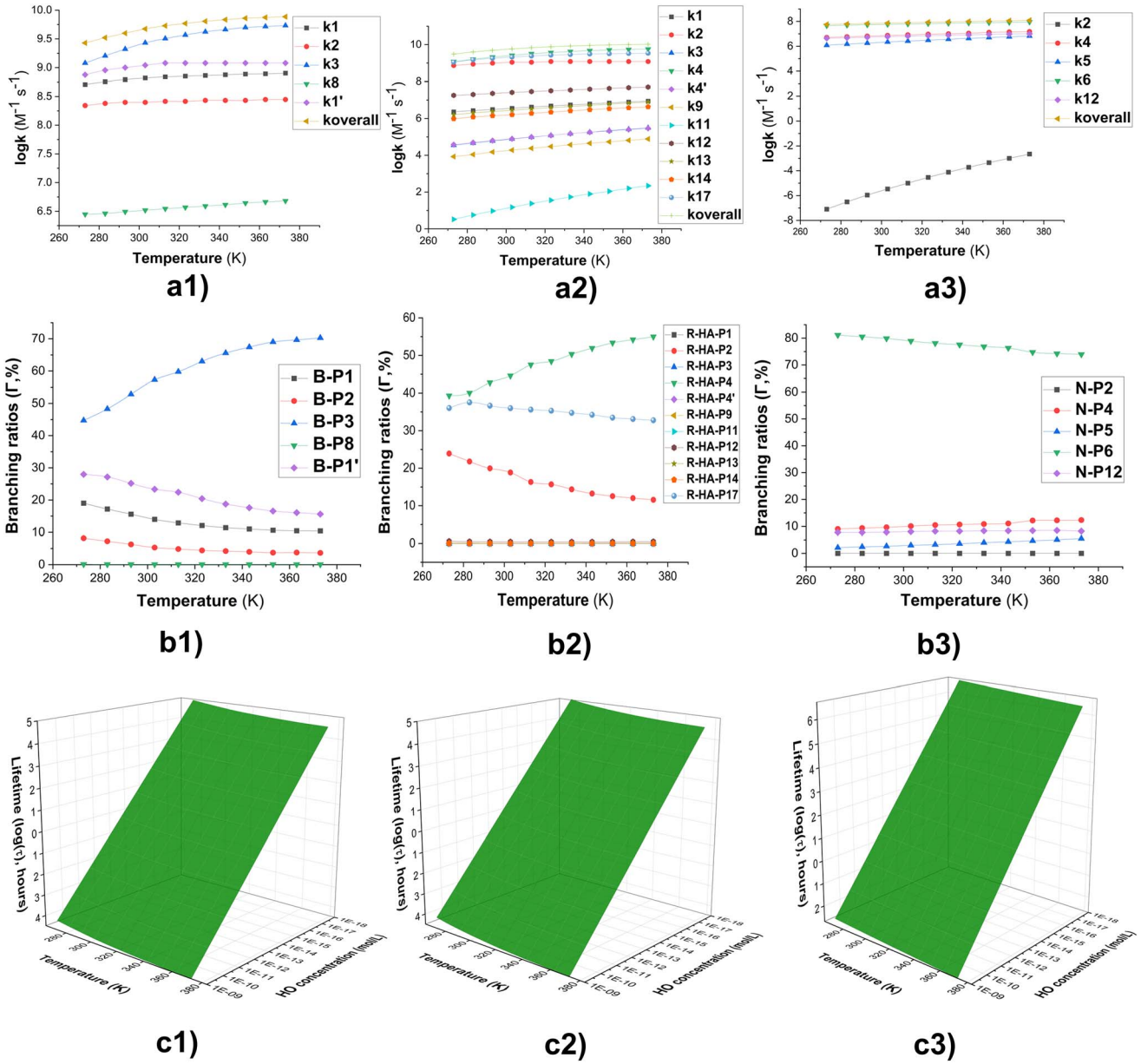

Fig. 6 (a) The temperature influence on apparent rate constants (log k); (b) Γ values (%); (c) lifetime (log(t), h) at 273–373 K ((1): BOD; (2): RDA-HA; (3): NPA-HA).

dominant route with branching ratios between 81.1% and 74.0% over the examined temperature range, while the C4 (**N-P4**) and C10 (**N-P10**) intermediates fluctuated within 9.0–12.3% and 7.8–8.2%, respectively.

The environmental lifetimes (τ) of the fluorophores under HO$^{\bullet}$ exposure were estimated over the temperature range of 273–373 K (Fig. 6c). Considering environmentally relevant hydroxyl radical concentrations 10^{-18} to 10^{-15} M in natural water, 10^{-10} to 10^{-9} M in AOP-treated wastewater,[21,70] the calculated lifetimes spanned from several hours to multiple years, depending on both radical concentration and temperature. For **BOD**, log(τ) decreased notably from 5.02 at 273 K to 1.55 at 373 K in natural waters. Similarly, **RDA-HA** lifetime also decreased, from 4.96 to 1.43. In contrast, **NPA** displayed relatively higher persistence, with log(τ) values of 6.69 at 273 K and 3.36 at 373 K, even under oxidative environments. Under AOP-treated wastewater conditions ([HO$^{\bullet}$] = 10^{-10} to 10^{-9} M), the degradation of **BOD** and **RDA-HA** was predicted to occur within seconds, whereas **NPA** decomposition would still require several minutes.

3.2. The reaction of fluorophores with HO$^{\bullet}$ in organic solvents

The degradation of **FPHs** by hydroxyl radicals was further investigated in organic solvents, namely methanol and pentyl ethanoate, to simulate conditions relevant to sensor applications in biological and lipid-like environments.[71–74] The kinetic parameters are summarized in Table 4 (methanol) and Table 5 (pentyl ethanoate).

Table 4 Calculated $\Delta G^{\ddagger}$ (kcal mol^{-1}), k_{Eck}, $k_{overall}$ (M^{-1} s^{-1}), k and Γ (%) of the reaction between HO$^{\bullet}$ and **FPHs** reactions at 298.15 K in methanol

		BOD			**RDA**			**NPA**		
Mechanism		$\Delta G^{\ddagger}$	k_{app}	Γ	$\Delta G^{\ddagger}$	k_{app}	Γ	$\Delta G^{\ddagger}$	k_{app}	Γ
FHT	N2–H							17.1	4.40	0.0
	N17–H				5.4	1.80×10^{9}	26.8			
RAF	C1	6.0	4.80×10^{8}	9.4	8.8	5.30×10^{6}	0.1			
	C1′	6.0	4.60×10^{8}	9.0						
	C2	6.2	3.40×10^{8}	6.7	5.4	1.10×10^{9}	16.4			
	C3	3.9	3.80×10^{9}	74.7	11.1	1.00×10^{5}	0.0			
	C4				3.5	3.80×10^{9}	56.5	8.2	1.50×10^{7}	12.7
	C4′				10.9	1.50×10^{5}	0.0			
	C5							9.1	3.10×10^{6}	2.6
	C6							7.2	8.20×10^{7}	69.4
	C8	8.2	6.70×10^{6}	0.1						
	C9				11.6	2.40×10^{4}	0.0			
	C10							8.1	1.80×10^{7}	15.2
	C11				15.8	1.90×10^{1}	0.0			
	C12				8.3	1.10×10^{7}	0.2			
	C13				9.2	2.80×10^{6}	0.0			
	C14				9.0	2.00×10^{6}	0.0			
$k_{overall}$			**5.09×10^{9}**			**6.72×10^{9}**			**1.18×10^{8}**	

As shown in Table 4, the overall rate constant of the **BOD** + HO$^{\bullet}$ reaction in methanol reached 5.09×10^{9} M^{-1} s^{-1}, with the C3 addition (**B-P3**) dominating at $\Gamma = 74.7\%$, followed by C1 (9.4%) and C1′ (9.0%). In pentyl ethanoate, $k_{overall}$ decreased to 1.38×10^{9} M^{-1} s^{-1}, and C3 addition became even more selective ($\Gamma = 86.9\%$), while C1 was the only notable secondary product ($\Gamma = 12.3\%$). Thus, **BOD** degrades efficiently in both solvents, with methanol leading to faster kinetics and pentyl ethanoate being more restrictive in the possible products.

For **RDA**, methanol introduced multiple competing pathways. The overall rate constant was high (6.72×10^{9} M^{-1} s^{-1}), with RAF at C4 ($\Gamma = 56.5\%$, **R-P4**), RAF at C2 ($\Gamma = 16.4\%$, **R-P2**), and FHT at N17–H ($\Gamma = 26.8\%$, **R-P17**) all contributing significantly. In pentyl ethanoate, however, the overall rate dropped to 1.16×10^{8} M^{-1} s^{-1}, nearly two orders of magnitude lower, while the dominant mechanism changed almost entirely to RAF. Specifically, C4 addition ($\Gamma = 64.4\%$) and C2 addition ($\Gamma = 29.2\%$) dominated, with FHT becoming negligible ($\Gamma < 5\%$). This demonstrates that proton-transfer channels are strongly solvent-dependent and suppressed in nonpolar media.

For **NPA**, reactivity was consistently lower than **BOD** and **RDA**. In methanol, $k_{overall}$ was 1.18×10^{8} M^{-1} s^{-1}, dominated by C6 addition ($\Gamma = 69.4\%$, **N-P6**), with secondary contributions from C10 (15.2%) and C4 (12.7%). In pentyl ethanoate, the

Table 5 Calculated $\Delta G^{\ddagger}$ (kcal mol^{-1}), k_{Eck}, $k_{overall}$ (M^{-1} s^{-1}), k and Γ (%) of the reaction between HO$^{\bullet}$ and **FPHs** reactions at 298.15 K in pentyl ethanoate

		BOD			**RDA**			**NPA**		
Mechanism		$\Delta G^{\ddagger}$	k_{app}	Γ	$\Delta G^{\ddagger}$	k_{app}	Γ	$\Delta G^{\ddagger}$	k_{app}	Γ
FHT	N2–H							16.1	1.00×10^{1}	0.0
	N17–H				10.8	5.50×10^{6}	4.7			
RAF	C1	6.7	1.70×10^{8}	12.3	10.5	3.70×10^{5}	0.3			
	C1′	8.8	4.60×10^{6}	0.3						
	C2	8.9	4.20×10^{6}	0.3	7.7	3.40×10^{7}	29.2			
	C3	5.3	1.20×10^{9}	86.9	14.4	4.50×10^{2}	0.0			
	C4				7.1	7.50×10^{7}	64.4	10.0	7.60×10^{5}	4.4
	C4′				13.1	3.90×10^{3}	0.0			
	C5							9.9	9.30×10^{5}	5.4
	C6							8.2	1.50×10^{7}	86.5
	C8	9.0	1.70×10^{6}	0.1						
	C9				13.6	8.50×10^{2}	0.0			
	C10							9.6	6.60×10^{5}	3.8
	C11				16.9	3.40	0.0			
	C12				9.9	9.00×10^{5}	0.8			
	C13				10.2	5.30×10^{5}	0.5			
	C14				10.7	1.10×10^{5}	0.1			
Total			**1.38×10^{9}**			**1.16×10^{8}**			**1.74×10^{7}**	

overall rate decreased further to 1.74×10^7 M^{-1} s^{-1}, with selectivity narrowing almost exclusively on C6 addition (Γ = 86.5% *vs.* C5 5.4% and C10 3.8%) became minor. Thus, solvent effects amplify the persistence of **NPA** and limit its product diversity.

Overall, the solvent dielectric constant has a strong effect on fluorophore degradation kinetics. In methanol, both **RDA** and **BOD** undergo fast decomposition with multiple pathways, whereas in lipid-like pentyl ethanoate, only **BOD** maintains high reactivity, while **RDA** and **NPA** degrade more slowly. This finding has practical implications: fluorescent labels intended for biological or lipid environments may exhibit enhanced stability (particularly **NPA**), whereas **BOD**-based probes are prone to rapid oxidative degradation across both hydrophilic and lipophilic conditions.

3.3. Environmental risk assessment

3.3.1. Ecological toxicity. The ecological toxicity of the **FPHs** and their hydroxyl radical-derived intermediates was evaluated against three representative aquatic species (fish, daphnids, and green algae), using acute (LC_{50}, EC_{50}) and chronic (ChV) endpoints. Fig. 7 presents the toxicity profiles as log(LC_{50}/EC_{50}/ChV, mg L^{-1}), where values < 2 indicate toxic effects, and lower values correspond to higher toxicity.[75]

For **BOD** and its primary degradation products (**B-P1**, **B-P1′**, **B-P2**, **B-P3**), the log(LC_{50}/EC_{50}/ChV) values are predicted to be consistently above 2, indicating low toxicity across all organisms. This suggests that **BOD**, despite its high reactivity with HO˙ radicals, and its major intermediates, are unlikely to pose significant acute or chronic ecological risks.

By contrast, **RDA** and its degradation intermediates are predicted to display strong toxicity potential. The parent species **RDA-H_2A**, **RDA-HA**, and neutral **RDA** all produced intermediates with log values < 2, notably **R-H_2A-P4**, **R-HA-P17**, and several neutral RAF products (**R-P2**, **R-P4**, **R-P5**, **R-P6**, **R-P9**). These results may indicate toxicity against all three tested organisms, particularly green algae and daphnid. Furthermore, the SET product (**R-P-SET**) is predicted to fall in the toxic range, underscoring the ecological risks associated with incomplete oxidative degradation of **RDA**.

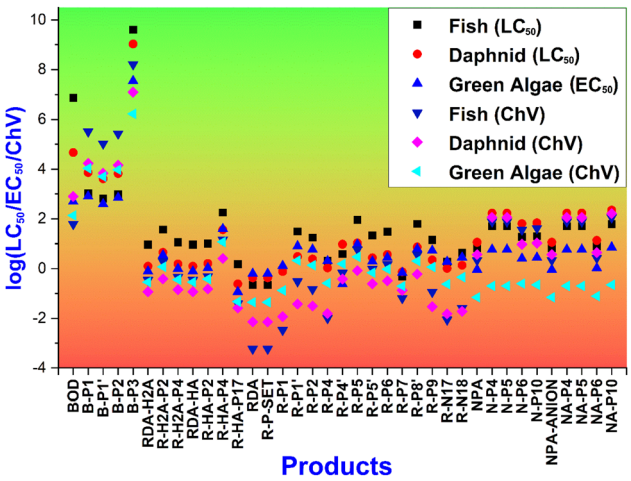

Fig. 7 Acute and chronic toxicity (log(LC_{50}/EC_{50}/ChV, mg L^{-1}) of FPHs and the main products.

For **NPA**, the neutral form and several RAF intermediates, including **N-P4**, **N-P6**, and **N-P10**, are predicted to exhibit values < 2, suggesting toxicity primarily toward algae. The anionic form of **NPA** and its associated products (**NA-P5**, **NA-P10**) also entered the toxic range, further emphasizing the role of pH in determining ecological risk.

Overall, the results highlight substantial differences among the three fluorophores. **BOD** and its products are ecologically benign, while **RDA** degradation is predicted to generate highly toxic intermediates, and **NPA** might exhibit moderate but pH-dependent toxicity. Therefore, it is critical to recognize that although hydroxyl radical attack accelerates fluorophore degradation, the process may simultaneously yield toxic intermediates, especially in the case of **RDA**. These findings underline the importance of coupling degradation efficiency assessments with toxicity evaluations when predicting the environmental fate of fluorophores.

3.3.2. Bioconcentration and biodegradability. The ecological risk posed by fluorophores depends not only on their reactivity and toxicity but also on their potential for bioaccumulation and biodegradation. Estimating bioconcentration factors (BCFs) provides a rational measure of organismal exposure to these chemicals and their degradation products.[76,77] Typically, compounds with BCF values above 5000 are considered to have high bioaccumulation potential.[78] The predicted BCF values of the studied fluorophores and their intermediates are summarized in Table S2, SI.

For **BOD** and its RAF-derived products (**B-P1**, **B-P1′**, **B-P2**, **B-P3**), BCF values were consistently low (≈3.16), far below the threshold for significant bioaccumulation. This result indicates that, despite their persistence in the aquatic environment, **BOD** and its breakdown products are unlikely to accumulate substantially in aquatic organisms. In contrast, **RDA** and its degradation intermediates are predicted to exhibit much higher BCF values. The parent neutral **RDA** and its SET-derived product (**R-P-SET**) reached values above 1400, while other products, such as **R-P7**, **R-P1**, and **R-P17**, fell in the range of 350–700. These values, although below the 5000 threshold, are several orders of magnitude greater than those of **BOD** and **NPA**, suggesting that **RDA** and its products may accumulate significantly in fish tissues and other organisms, thereby elevating ecological risk. For **NPA** and its products, both the neutral and anionic forms showed low BCF values (≈9.6), and all intermediates (**N-P4**, **N-P5**, **N-P6**, **N-P12**, **NA-P4**, **NA-P5**, **NA-P6**, **NA-P10**) remained below 5. These results suggest that **NPA**, similar to **BOD**, does not present substantial bioaccumulation potential.

The biodegradability of these fluorophores was evaluated using the BIOWIN 3, 4, and 5 models in EPI Suite,[64] (Table S2, SI). The results indicate that all parent compounds and their major products are non-biodegradable, with degradation timelines extending from weeks to months. While some initial biodegradation may occur, the persistence of both the reactants and their intermediates is predicted to be high.

In summary, although **BOD** and **NPA** do not accumulate in living organisms, their poor biodegradability suggests that they may persist in aquatic systems. **RDA** and its intermediates are predicted to present the most severe concern, combining poor biodegradability with relatively high BCF values, thus posing the greatest long-term ecological hazard among the three fluorophore systems.

4. Conclusion

A comprehensive computational investigation was conducted to assess the hydroxyl radical-driven degradation pathways of three common fluorophores: **RDA**, **NPA**, and **BOD**. These fluorophores have markedly different reactivities and thus varying environmental lifetimes, ranging from a few hours for neutral **RDA** to several months or years for neutral **NPA**. The radical degradation predominantly proceeds *via* the RAF and FHT mechanisms, while the SET pathway also contributes to neutral **RDA**. The protonation states determine the degradation pathways of **RDA** and **NPA** but do not affect the degradation of **BOD**. It was established that **RAD**, **NPA** and their intermediates are predicted to exhibit high ecotoxicity ($\log LC_{50}/EC_{50}/ChV < 2$), poor biodegradability, and strong bioaccumulation potential, whereas the degradation products of **BOD** are expected to be less toxic and more environmentally benign despite their persistence. Overall, the study yielded a hazard ranking of **RDA** $\approx$ **NPA** > **BOD**, underscoring that although hydroxyl radical oxidation efficiently progresses fluorophore degradation, it may simultaneously generate harmful by products.

Conflicts of interest

There are no conflicts to declare.

Data availability

The data supporting this article have been included as part of the supplementary information (SI). Supplementary information is available. See DOI: https://doi.org/10.1039/d6ra00906a.

Acknowledgements

This research is funded by the Vietnamese Ministry of Education and Training under project number B2025.DNA.02.

References

1 Z. G. Song, Q. Yuan, P. Lv and K. Chen, *Sensors*, 2021, **21**, 6326.
2 Y. Jeong and J. Yoon, *Inorg. Chim. Acta*, 2012, **381**, 2–14.
3 D. Wu, A. C. Sedgwick, T. Gunnlaugsson, E. U. Akkaya, J. Yoon and T. D. James, *Chem. Soc. Rev.*, 2017, **46**, 7105–7123.
4 Y. Wang, X. Wang, W. Ma, R. Lu, W. Zhou and H. Gao, *Chemosensors*, 2022, **10**, 399.
5 M. Beija, C. A. Afonso and J. M. Martinho, *Chem. Soc. Rev.*, 2009, **38**, 2410–2433.
6 H. N. Kim, M. H. Lee, H. J. Kim, J. S. Kim and J. Yoon, *Chem. Soc. Rev.*, 2008, **37**, 1465–1472.
7 N. Jain and N. Kaur, *Coord. Chem. Rev.*, 2022, **459**, 214454.
8 H.-Q. Dong, T.-B. Wei, X.-Q. Ma, Q.-Y. Yang, Y.-F. Zhang, Y.-J. Sun, B.-B. Shi, H. Yao, Y.-M. Zhang and Q. Lin, *J. Mater. Chem. C*, 2020, **8**, 13501–13529.
9 H. Xu, Y. Xiao, Y. G. Liu and W. Sun, *Adv. Sens. Res.*, 2023, **3**, 2300032.
10 V. Grover and M. Ravikanth, *Tetrahedron Chem*, 2025, **13**, 100121.
11 N. Boens, V. Leen and W. Dehaen, *Chem. Soc. Rev.*, 2012, **41**, 1130–1172.
12 T. Kowada, H. Maeda and K. Kikuchi, *Chem. Soc. Rev.*, 2015, **44**, 4953–4972.
13 G. Ulrich, R. Ziessel and A. Harriman, *Angew. Chem., Int. Ed.*, 2008, **47**, 1184–1201.
14 R. Ziessel, G. Ulrich and A. Harriman, *New J. Chem.*, 2007, **31**, 496.
15 S. O. Fakayode, C. Lisse, W. Medawala, P. N. Brady, D. K. Bwambok, D. Anum, T. Alonge, M. E. Taylor, G. A. Baker, T. F. Mehari, J. D. Rodriguez, B. Elzey, N. Siraj, S. Macchi, T. Le, M. Forson, M. Bashiru, V. E. Fernand Narcisse and C. Grant, *Appl. Spectrosc. Rev.*, 2023, **59**, 1–89.
16 R. Sivakumar and N. Y. Lee, *BioChip J.*, 2021, **15**, 216–232.
17 P. P. Vaughan and N. V. Blough, *Environ. Sci. Technol.*, 1998, **32**, 2947–2953.
18 K. Takeda, H. Takedoi, S. Yamaji, K. Ohta and H. Sakugawa, *Anal. Sci.*, 2004, **20**, 153–158.
19 H. Xu, Y. Li, J. Liu, H. Du, Y. Du, Y. Su and H. Jiang, *Water Res.*, 2020, **176**, 115774.
20 S. A. Timko, C. Romera-Castillo, R. Jaffé and W. J. Cooper, *Environ. Sci.: Processes Impacts*, 2014, **16**, 866–878.
21 D. Vione, G. Falletti, V. Maurino, C. Minero, E. Pelizzetti, M. Malandrino, R. Ajassa, R.-I. Olariu and C. Arsene, *Environ. Sci. Technol.*, 2006, **40**, 3775–3781.
22 J. L. Wang and L. J. Xu, *Crit. Rev. Environ. Sci. Technol.*, 2012, **42**, 251–325.
23 Y. Nosaka and A. Nosaka, *ACS Energy Lett.*, 2016, **1**, 356–359.
24 S. Gligorovski, R. Strekowski, S. Barbati and D. Vione, *Chem. Rev.*, 2015, **115**, 13051–13092.
25 Q. V. Vo, L. T. T. Thao, T. D. Manh, M. V. Bay, B. T. Truong-Le, N. T. Hoa and A. Mechler, *RSC Adv.*, 2024, **14**, 27265–27273.
26 J. Zhu, H. Wang, A. Duan and Y. Wang, *J. Hazard. Mater.*, 2023, **446**, 130676.
27 X. Bo, J. Sun, Q. Mei, B. Wei, Z. An, Z. Qiu, D. Han, J. Xie and M. He, *J. Cleaner Prod.*, 2021, **293**, 126161.
28 Z. An, X. Bo, Q. Mei, B. Wei, J. Xie, J. Zhan and M. He, *Sci. Total Environ.*, 2022, **816**, 151651.
29 F. Y. Bai, S. Ni, Y. Z. Tang, X. M. Pan and Z. Zhao, *Sci. Total Environ.*, 2020, **699**, 134190.
30 Y. Sun, M. Li, M. H. Hadizadeh, L. Liu and F. Xu, *J. Environ. Sci.*, 2023, **129**, 189–201.
31 M. J. Frisch, G. W. Trucks, H. B. Schlegel, G. E. Scuseria, M. A. Robb, J. R. Cheeseman, G. Scalmani, V. Barone, B. Mennucci, G. A. Petersson, H. Nakatsuji, M. Caricato, X. Li, H. P. Hratchian, A. F. Izmaylov, G. Z. J. Bloino,

J. L. Sonnenberg, M. Hada, M. Ehara, K. Toyota, R. Fukuda, J. Hasegawa, M. Ishida, T. Nakajima, Y. Honda, O. Kitao, H. Nakai, T. Vreven, J. A. Montgomery Jr., J. E. Peralta, F. Ogliaro, M. Bearpark, J. J. Heyd, E. Brothers, K. N. Kudin, V. N. Staroverov, T. Keith, R. Kobayashi, J. Normand, K. Raghavachari, A. Rendell, J. C. Burant, S. S. Iyengar, J. Tomasi, M. Cossi, N. Rega, J. M. Millam, M. Klene, J. E. Knox, J. B. Cross, V. Bakken, C. Adamo, J. Jaramillo, R. Gomperts, R. E. Stratmann, O. Yazyev, A. J. Austin, R. Cammi, C. Pomelli, J. W. Ochterski, R. L. Martin, K. Morokuma, V. G. Zakrzewski, G. A. Voth, P. Salvador, J. J. Dannenberg, S. Dapprich, A. D. Daniels, O. Farkas, J. B. Foresman, J. V. Ortiz, J. Cioslowski and D. J. Fox, *Gaussian 16*, Gaussian, Inc., Wallingford, CT, 2016.

32 M. Carreon-Gonzalez, A. Vivier-Bunge and J. R. Alvarez-Idaboy, *J. Comput. Chem.*, 2019, 2103–2110.

33 N. Mora-Diez, J. R. Alvarez-Idaboy and R. J. Boyd, *J. Phys. Chem. A*, 2001, **105**, 9034–9039.

34 A. Galano and J. R. Alvarez-Idaboy, *J. Comput. Chem.*, 2014, **35**, 2019–2026.

35 C. Kalalian, G. El Dib, H. Singh, P. Rao, E. Roth and A. Chakir, *Atmos. Environ.*, 2020, **223**, 117306.

36 C. Kalalian, A. Grira, J. N. Illmann, I. Patroescu-Klotz, G. El Dib, P. Coddeville, A. Canosa, P. Wiesen, B. Aazaad and L. Senthilkumar, *Atmosphere*, 2022, **13**, 291.

37 N. Schaeffer, J. H. Conceição, M. A. Martins, M. C. Neves, G. Pérez-Sánchez, J. R. Gomes, N. Papaiconomou and J. A. Coutinho, *Green Chem.*, 2020, **22**, 2810–2820.

38 T. L. Galvão, A. Kuznetsova, J. R. Gomes, M. L. Zheludkevich, J. Tedim and M. G. Ferreira, *Theor. Chem. Acc.*, 2016, **135**, 78.

39 J. R. l. Alvarez-Idaboy and A. Galano, *J. Phys. Chem. B*, 2012, **116**, 9316–9325.

40 Y. Zhao and D. G. Truhlar, *Theor. Chem. Acc.*, 2008, **120**, 215–241.

41 E. Dzib, J. L. Cabellos, F. Ortíz-Chi, S. Pan, A. Galano and G. Merino, *Int. J. Quantum Chem.*, 2019, **119**, e25686.

42 A. V. Marenich, C. J. Cramer and D. G. Truhlar, *J. Phys. Chem. B*, 2009, **113**, 6378–6396.

43 M. E. Alberto, N. Russo, A. Grand and A. Galano, *Phys. Chem. Chem. Phys.*, 2013, **15**, 4642–4650.

44 W. Li, Y. Shang, H. Ning, J. Li and S.-N. Luo, *Phys. Chem. Chem. Phys.*, 2020, **22**, 5797–5806.

45 A. Galano, G. Mazzone, R. Alvarez-Diduk, T. Marino, J. R. Alvarez-Idaboy and N. Russo, *Annu. Rev. Food Sci. Technol.*, 2016, **7**, 335–352.

46 M. G. Evans and M. Polanyi, *Trans. Faraday Soc.*, 1935, **31**, 875–894.

47 H. Eyring, *J. Chem. Phys.*, 1935, **3**, 107–115.

48 D. G. Truhlar, W. L. Hase and J. T. Hynes, *J. Phys. Chem.*, 1983, **87**, 2664–2682.

49 T. Furuncuoglu, I. Ugur, I. Degirmenci and V. Aviyente, *Macromolecules*, 2010, **43**, 1823–1835.

50 E. Vélez, J. Quijano, R. Notario, E. Pabón, J. Murillo, J. Leal, E. Zapata and G. Alarcón, *J. Phys. Org. Chem.*, 2009, **22**, 971–977.

51 E. Dzib, J. L. Cabellos, F. Ortiz-Chi, S. Pan, A. Galano and G. Merino, *Eyringpy 1.0.2*, Cinvestav, Mérida, Yucatán, 2018.

52 C. Eckart, *Phys. Rev.*, 1930, **35**, 1303.

53 E. Pollak and P. Pechukas, *J. Am. Chem. Soc.*, 1978, **100**, 2984–2991.

54 A. Fernández-Ramos, B. A. Ellingson, R. Meana-Pañeda, J. M. Marques and D. G. Truhlar, *Theor. Chem. Acc.*, 2007, **118**, 813–826.

55 B. N. Ames, M. K. Shigenaga and T. M. Hagen, *Proc. Natl. Acad. Sci. U. S. A.*, 1993, **90**, 7915–7922.

56 A. Galano and J. Raúl Alvarez-Idaboy, *Int. J. Quantum Chem.*, 2019, **119**, e25665.

57 Q. V. Vo, T. L. B. Tram, N. T. Hoa, A.-N. Au-Duong and A. Mechler, *Polym. Degrad. Stab.*, 2023, **216**, 110483.

58 M. Li, J. Sun, Q. Mei, B. Wei, Z. An, H. Cao, C. Zhang, J. Xie, J. Zhan and W. Wang, *J. Hazard. Mater.*, 2021, **416**, 126250.

59 Q. Mei, J. Sun, D. Han, B. Wei, Z. An, X. Wang, J. Xie, J. Zhan and M. He, *Chem. Eng. J.*, 2019, **373**, 668–676.

60 J. Sun, B. Wei, Q. Mei, Z. An, X. Wang and M. He, *Chem. Eng. J.*, 2019, **358**, 456–466.

61 S. Luo, Z. Wei, D. D. Dionysiou, R. Spinney, W.-P. Hu, L. Chai, Z. Yang, T. Ye and R. Xiao, *Chem. Eng. J.*, 2017, **327**, 1056–1065.

62 Y. Gao, Y. Ji, G. Li and T. An, *Water Res.*, 2016, **91**, 77–85.

63 N. T. Hoa and Q. V. Vo, *Chemosphere*, 2023, **314**, 137682.

64 R. S. Boethling, D. G. Lynch, J. S. Jaworska, J. L. Tunkel, G. C. Thom and S. Webb, *Environ. Toxicol. Chem.*, 2004, **23**, 911–920.

65 *ChemAxon*, 2025, https://www.chemaxon.com.

66 M. Xu, J. Yao, S. Sun, S. Yan and J. Sun, *Toxics*, 2021, **9**, 234.

67 J. Sun, B. Wei, Q. Mei, Z. An, X. Wang, D. Han, J. Xie, J. Zhan, Q. Zhang, W. Wang and M. He, *Chem. Eng. J.*, 2020, **382**, 122791.

68 D. Dwinandha, B. Zhang and M. Fujii, *Chemosphere*, 2022, **291**, 132763.

69 J. I. Mujika, J. Uranga and J. M. Matxain, *Chem.–Eur. J.*, 2013, **19**, 6862–6873.

70 J. M. Burns, W. J. Cooper, J. L. Ferry, D. W. King, B. P. DiMento, K. McNeill, C. J. Miller, W. L. Miller, B. M. Peake and S. A. Rusak, *Aquat. Sci.*, 2012, **74**, 683–734.

71 L. Gopala, Y. Cha and M. H. Lee, *Dyes Pigm.*, 2022, **201**, 110195.

72 O. S. Vodyanova, B. A. Kochergin, S. D. Usoltsev, Y. S. Marfin, E. V. Rumyantsev, E. L. Aleksakhina and I. K. Tomilova, *J. Photochem. Photobiol., A*, 2018, **350**, 44–51.

73 T. Jia, C. Fu, C. Huang, H. Yang and N. Jia, *ACS Appl. Mater. Interfaces*, 2015, **7**, 10013–10021.

74 M. Asano, M. Doi, K. Baba, M. Taniguchi, M. Shibano, S. Tanaka, M. Sakaguchi, M. Takaoka, M. Hirata, R. Yanagihara, R. Nakahara, Y. Hayashi, T. Yamaguchi, H. Matsumura and Y. Fujita, *J. Biosci. Bioeng.*, 2014, **118**, 98–100.

75 P. Reuschenbach, M. Silvani, M. Dammann, D. Warnecke and T. Knacker, *Chemosphere*, 2008, **71**, 1986–1995.

76 J. A. Arnot and F. A. P. C. Gobas, *Environ. Rev.*, 2006, **14**, 257–297.

77 L. P. Burkhard, *Environ. Toxicol. Chem.*, 2021, **40**, 1530–1543.

78 M. J. He, X. J. Luo, M. Y. Chen, Y. X. Sun, S. J. Chen and B. X. Mai, *Sci. Total Environ.*, 2012, **419**, 109–115.